

## Directional coupling in dual-branch electron-waveguide junctions

O. Vanbésien and D. Lippens

*Institut d'Electronique et de Microélectronique du Nord UMR CNRS9929, Département Hyperfréquences et Semiconducteurs, Domaine Universitaire de Lille, Avenue Poincaré, Boîte Postale 69, F-59652 Villeneuve d'Ascq Cédex, France*

(Received 8 March 1995; revised manuscript received 23 May 1995)

We present a detailed analysis of a quantum directional coupler. The innovative aspect of the proposal comes from a dual coupling scheme. With respect to structures with a single interaction window, the crucial advantage is that the phase in the output leads can be strongly modulated through the distinct coupling paths. As a consequence, the proposed structure is highly directional in a four-terminal configuration. In order to address the above idea, a theoretical analysis is conducted by solving the two-dimensional Schrödinger equation using a mode-matching technique. Transmission spectra and conductance variations are calculated and interpreted paying attention to the influence of structural parameters such as wire widths and branch-line coupling lengths. On this basis, a parametric analysis is carried out including notably studies of the multimode operation and of the influence of electrostatic potential variations along the direction of propagation. Various modes of operation are pointed out. First, we illustrate a 3-dB coupling situation with a directivity as high as 35 dB in the monomode limit where the clearest interference effects are expected. Second, a real-space transfer mechanism with over 90% of transferred electrons is proposed as the operating mechanism of a quantum interference electronic switch. At last, the time response of mechanisms is discussed by viewing the transfer of electrons as a resonance process.

### I. INTRODUCTION

Electronic transport in confined semiconductor geometries has received increasing interest in the last decade with the potential of a new class of quantum devices whose functionality appears promising for the future. Since the pioneering works of Tsu and Esaki<sup>1,2</sup> on superlattices and double-barrier resonant tunneling heterostructures,<sup>3-5</sup> quantum size and tunneling effects<sup>6-12</sup> have been thoroughly studied in multilayered structures grown mainly by molecular-beam epitaxy. Recently, advances in electron lithography technique at the nanometer scale have made it possible to control the lateral extent of a two-dimensional electron gas created at the interface of a modulation-doped heterojunction in such a way that the motion of carriers is restricted to one direction. Furthermore, if the length of these quasi-one-dimensional microstructures is less than the phase-coherence length over which the electrons retain phase information, the transport is ballistic, with conduction properties solely determined by the geometry of structures. In this regard, the material of choice is the modulation-doped  $\text{Al}_x\text{Ga}_{1-x}\text{As}/\text{GaAs}$  heterostructure where electron mobility as high as  $10^6 \text{ cm}^2 \text{ V}^{-1} \text{ s}^{-1}$  has been measured<sup>13</sup> in liquid helium with the associated benefit of a coherence length on the order of a micrometer. Under these conditions and due to transverse quantum effects in the waveguide, conductance quantization has been revealed by varying the dimensions of the quantum wire by means of gate bias. Experimentally, plateau-like structures are obtained in the current-voltage characteristics which have been vastly reported and analyzed in the literature.<sup>14-28</sup>

A next step in the understanding of electron transport

in the waveguide is to study junctions.<sup>29-35</sup> Therefore, T-shaped structures, acting as a lateral stub,<sup>29</sup> and directional couplers by analogy with optics and microwave components have been considered. For the latter, several proposals have been analyzed including structures with a middle extremely narrow gate which controls the height and width of a tunneling barrier between two waveguides in close proximity,<sup>30</sup> or with an open window region induced by a split gate.<sup>34</sup> In this paper, we propose and analyze theoretically a directional coupler which consists of two parallel quantum wires coupled by two branch lines. The crucial advantage of such a coupling scheme is that the phase of electrons in the output leads can be strongly modulated through the different coupling paths. As a consequence the proposed structure is highly directional in a four-terminal configuration. In order to support this idea, a theoretical study was carried out using mode-matching techniques. This numerical procedure was developed originally by Kühn<sup>36</sup> to compute electromagnetic fields inside multiports waveguide circuits, and was used recently by Weisshaar *et al.*<sup>37,38</sup> for quantum structures such as bent narrow wires. For the present work, this approach was extended to the case of four-terminal systems in order to determine, by solving the two-dimensional Schrödinger equation, the wave function within each region constituting the coupler. The transmission characteristics are first calculated, and conductance spectra are then deduced according to the Landauer-Büttiker formula.<sup>39,40</sup> By varying systematically the bias conditions and topology of structures, various operating modes have been revealed which can give rise to concepts of devices whose operations rely entirely on interference effects. First of all, a directional coupling<sup>41</sup> effect with a directivity as high as 35 db with a quasiequal

share of the presence probabilities at the two coupled output ports was found in the single-mode limit where the clearest quantum-mechanical effects are expected. Also, a real-space transfer with an electron transfer exceeding 90% was demonstrated, and is proposed as the operating mechanism of a quantum interference switch.<sup>42</sup>

The paper is organized as follows: Theoretical aspects along with the calculation of the transmission, conductance, and coupling characteristics, described by the coupling and directivity coefficients, are presented in Sec. II. Section III is devoted to a parametric study related to the influence of the structure geometry, bias conditions, and properties of coupled waveguides in multimode operation. Also, a comparison between a single and a double branch coupler is presented. Finally, the various regimes of operation are analyzed and discussed with a first approach of the time response of phenomena by viewing the charge transfer as a resonant tunneling process. Section IV contains concluding remarks.

## II. THEORETICAL ANALYSIS

Basically, there are two ways to couple two-electron waveguides. First, one can make use of a very thin tunneling barrier as was proposed in earlier works. Such a coupling scheme can be achieved by means of a very narrow gate on the surface of a modulation-doped heterostructure with a bias control of the coupling between the two waveguides. A second procedure consists of using an open interaction window, as considered in the present paper. In practice, this can be implemented by means of split gates. Figure 1 depicts such a scheme in a four-terminal configuration. Instead of a hole or slit used as a coupling structure, the interconnecting regions have sizable dimensions with respect to the electron wavelength. Hence, we will use the phrase “branch line coupler” in the sense that the coupling regions behave as electron waveguide sections with their own propagation characteristics. This also means that it is possible to operate in a tunneling (coupling by evanescent waves) or propagating mode according to the geometry and the energy range considered. Also of major concern is the directivity of the structures. By analogy with a directional microwave coupler, the directivity can be defined as a measure of the unbalance between the electromagnetic waves

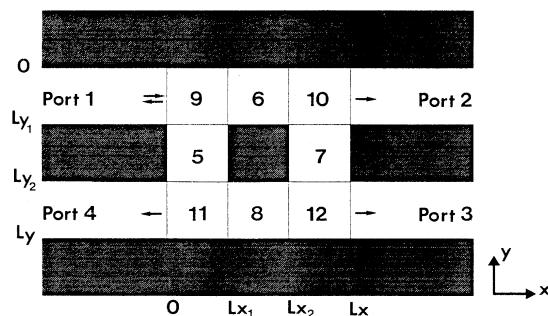


FIG. 1. Topology of the quantum directional coupler with two branch lines.

at the output ports of the coupled waveguide (let us say between ports 3 and 4) according to the notation of Fig. 1, by assuming a structure fed by port 1. From this point of view, a single interaction window with an opening at the nanometer scale is not directional, as shown below. In contrast, a dual-branch scheme can overcome this drawback with a degree of freedom in the control of the presence probability afforded by the two distinct coupling paths. However, other operating modes can also be found notably with a complete change in the propagation direction and hence with a drastic unbalance between adjacent wires. Concerning ways to show the effects of directional coupling, we have a choice between several theoretical approaches. Therefore, the transport properties can be investigated by studying the time evolution of a Gaussian wave packet initialized in one arm of the directional coupler impinging successively on the two branches and interacting with them. By means of this procedure, based on solving the time-dependent Schrödinger equation, resonant charge transfer can be demonstrated and the time response of the mechanism involved can be analyzed. In counterpart, due to the fact that the Gaussian wave packet exhibits a spread in energy, it appears relatively difficult to calculate quantities relevant to the coupling of the structure except by integration. This difficulty can be ruled out with the spectroscopic method. Indeed, by analyzing the quantum state of the whole structure as the solution of the time-independent Schrödinger equation, the transmission probability can be determined very accurately for each electron energy value, and hence the coupling characteristics. Moreover, it is possible to obtain an estimate of the time response mechanism involved from the broadening of the resonance peaks, as is done for conventional resonant tunneling structures.

### A. Wave-function calculation

A two-dimensional approach is used to solve the time-independent Schrödinger equation in the effective-mass approximation. In order to suggest what features are related to the interference phenomena, analysis was made in the ideal case of hard walls and square corner waveguides. In a previous work it was verified that the directivity inherent to the double-branch scheme still holds when a more realistic shape is assumed.<sup>43</sup> In addition, since in general the clearest quantum-mechanical effects are expected in the single-mode regime, we choose typical wire widths around 20 nm in order to preserve a monomode operation over a relatively broad energy range. Finally, assuming that the electron coherence length is longer than the size of the device (180 nm here) we treat the transport ballistically. In each subregion defined by the grid in Fig. 1, the wave function is expanded in orthogonal functions with propagating or evanescent properties, according to the energy considered, weighted by harmonic terms describing the quantized effects in the transverse direction. The solution can be thus written in the following form:

$$\Psi(x,y) = \sum_m \left[ \frac{2}{w} \right]^{1/2} \sin \left[ \frac{m\pi}{w} y \right] \times \left[ A_m e^{\gamma_m x} + B_m e^{-\gamma_m x} \right], \quad (1)$$

with

$$\gamma_m = \left[ \frac{2m^*}{\hbar^2} E - \left[ \frac{m\pi}{w} \right]^2 \right]^{1/2}. \quad (2)$$

In these expressions,  $w$  is the width of the square confining potential with quantum levels indexed by  $m$ , and  $\gamma_m$  is the propagation or attenuation constant [evanescent modes depending on the sign of the term under square root in Eq. (2)] along the direction of propagation.

Now considering in more detail the topology of the coupler, we partition the structure into 12 regions where the wave function can be written independently using different expressions of Eq. (1), namely, two waveguides (regions labeled 1-9-6-10-2 and 4-11-8-12-3) connected by two branch lines (regions 9-5-11 and 10-7-12). We thus obtain three different forms for the wave function since regions 1-2-3-4 (type A), regions 5-6-7-8 (type B), and regions 9-10-11-12 (type C) are equivalent owing to variable

and index transformations.

In region 1 (type A), the wave function is written as

$$\Psi^1 = \sum_m (a_m^1 e^{\gamma_m^1 x} + b_m^1 e^{-\gamma_m^1 x}) \sin \left[ \frac{m\pi}{Ly_1} y \right]. \quad (3)$$

In the following, we will assume a feeding of the structure by port 1 with unitary presence probability. Hence, due to reflections in the interconnecting regions, the wave function is the sum of a forward wave and a backward wave. Conversely, for the other three ports (2-3-4), only waves leaving the simulation domain are computed. This means that no waves are incoming from these three ports considered as output terminals, and which thus behave as perfect matching loads. In practice, this could be achieved by an offset of the chemical potentials at terminals 2, 3, and 4 with respect to terminal 1 so that the charge transfers at the Fermi level at the output ports are forbidden.

In the coupling region (from 5 to 12), the wave function is constructed by placing successively hard walls at all  $-1$  open boundaries and by superimposing the different solutions thus obtained. This procedure gives a suitable set of orthogonal functions for the application of mode matching. For region 5 (type B) we obtain

$$\Psi^5 = \sum_m \left[ d_m^{a5} \sinh[\beta_m^5 (y - Ly_2)] \sin \left[ \frac{m\pi}{Lx_1} x \right] + d_m^{b5} \sinh[\beta_m^5 (y - Ly_1)] \sin \left[ \frac{m\pi}{Lx_1} x \right] \right] \quad (4)$$

where the coefficients  $d^a$  and  $d^b$  correspond to the two superimpositions necessary in that case (two open boundaries), and  $Ly_i$  and  $Lx_i$  are marked in Fig. 1. For region 9 (type C), we have

$$\Psi^9 = \sum_m \left[ e_m^{a9} \sinh[\gamma_m^9 (x - Lx_1)] \sin \left[ \frac{m\pi}{Ly_1} y \right] + e_m^{b9} \sinh(\beta_m^9 y) \sin \left[ \frac{m\pi}{Lx_1} x \right] + e_m^{c9} \sinh(\gamma_m^9 x) \sin \left[ \frac{m\pi}{Ly_1} y \right] \right] \quad (5)$$

with coefficients  $e^a$ ,  $e^b$ , and  $e^c$  to account for the three open boundaries.

In order to calculate the amplitude of the wave functions in each region, we first apply the continuity equation of the wave function  $\psi$ , and second impose the continuity of the normal derivative of  $\psi$  at each interface. Again, only two series of fundamentally different equations are found for interfaces of types A-C and type B-C, respectively.

As an example, for interface 1-9 (type A-C) the continuity conditions are expressed as

$$\forall m \ a_m^1 + b_m^1 = -e_m^{a9} \sinh(\gamma_m^9 Lx_1) \quad (6)$$

and

$$\forall m \ \gamma_m^1 (a_m^1 - b_m^1) = e_m^{a9} \gamma_m^9 \cosh(\gamma_m^9 Lx_1) + \sum_{n=1}^{\infty} e_n^{b9} \frac{2n\pi}{Lx_1 Ly_1} K_{n,m}^1 + \gamma_m^9 e_m^{c9}$$

with

$$K_{n,m}^1 = \int_0^{Ly_1} \sinh(\beta_n^9 y) \sin \left[ \frac{m\pi}{Ly_1} y \right] dy. \quad (7)$$

Concerning interface 9-5 (type B-C), we obtain

$$\forall m \ e_m^{b9} \sinh(\beta_m^9 Ly_1) = d_m^{a5} \sinh[\beta_m^5 (Ly_1 - Ly_2)] \quad (8)$$

and

$$\forall m \ \sum_{n=1}^{\infty} \frac{2n\pi(-1)^n}{Ly_1 Lx_1} (e_n^{a9} L_{n,m}^1 + e_n^{c9} L_{n,m}^2) + e_m^{b9} \beta_m^9 \cosh(\beta_m^9 Ly_1) = d_m^{a5} \beta_m^5 \cosh[\beta_m^5 (Ly_1 - Ly_2)] + d_m^{b5} \beta_m^5 \quad (9)$$

with

$$L_{n,m}^1 = \int_0^{Lx_1} \sinh[\gamma_n^9(x - Lx_1)] \sin\left[\frac{m\pi}{Lx_1}x\right] dx \quad (9)$$

and

$$L_{n,m}^2 = \int_0^{Lx_1} \sinh(\gamma_n^9 x) \sin\left[\frac{m\pi}{Lx_1}x\right] dx .$$

By applying this procedure to the 12 interfaces, a set of linear equations (dimension  $24N \times 24N$ , where  $N$  is the number of quantum levels or modes considered in the simulation) is obtained which interrelates the amplitude coefficients of the wave function to the known values  $a_m^1$  which described the incident waves at port 1. In order to obtain a less time-consuming code, all  $e_m^{ai}$ ,  $e_m^{bi}$ , and  $e_m^{ci}$  ( $i=9, 10, 11$ , and  $12$ ) are analytically eliminated to finally obtain a  $12N \times 12N$  matrix  $M$ . The amplitude coefficients of the wave functions in the remaining regions stored in vector  $X$  are given by

$$X = M^{-1}B, \quad (10)$$

where the column matrix  $B$  contains the amplitude coefficients of the wave function in region 1. This infinite set of equations has to be truncated in order to obtain numerical solutions. For example, when all dimensions such as waveguide widths or coupling lengths are kept smaller than 60 nm, satisfactory convergence is obtained provided 20 modes are included in the simulation.

### B. Transmission, conductance, and coupling characteristics

Using the amplitude coefficients calculated with the method outlined above, it is now possible to calculate the transmissivity properties for a four-port structure. Therefore, the transmission coefficient at port  $i$  ( $i=2, 3$ , and  $4$ ) for incident mode  $j$ , by taking into account  $N$  modes in the coupling region can be obtained by

$$T_{1,i}^j = \sum_{m=1}^N b_m^i b_m^{i*} (\gamma_m^i - \gamma_m^{i*}) / a_j^1 a_j^{1*} (\gamma_j^1 - \gamma_j^{1*}). \quad (11)$$

The reflection coefficient at port 1 is calculated in the same way:

$$R_1^j = \sum_{m=1}^N b_m^1 b_m^{1*} (\gamma_m^1 - \gamma_m^{1*}) / a_j^1 a_j^{1*} (\gamma_j^1 - \gamma_j^{1*}). \quad (12)$$

Experimentally, for split-gate structures, only the conductance information can be measured by varying gate voltages and thus constricting more or less efficiently the electron gas in the quantum waveguide by a modulation of their widths. In the limit of zero temperature and low-bias voltages between input and output ports, the conductance at each port is expressed according to Landauer and Büttiker's formulation:

$$G_i = \frac{2e^2}{h} \sum_{j=1}^K T_{1,i}^j(E_F), \quad i=2,3,4. \quad (13)$$

Here the summation is performed on the number  $K$  of

propagating modes at the energy  $E_F$  corresponding to the Fermi level in the incident waveguide.

In analogy with microwave couplers, we subsequently define the directivity as the ratio of presence probability between ports 3 and 4, whereas the coupling coefficient reflects the sharing of the wave function between the incident ports 1 and 3. Numerically, the directivity ( $D$ ) and coupling coefficients ( $C$ ) are expressed using the conductance terms, respectively:

$$D_{\text{dB}} = 10 \log_{10}(G_4/G_3) \quad (14)$$

and

$$C_{\text{dB}} = 10 \log_{10}(G_4/K), \quad (15)$$

where  $K$  is the number of incident propagating modes whose amplitudes are normalized to unity.

## III. RESULTS AND DISCUSSION

### A. Transmission spectra

Figure 2 shows a typical result of the variations of the transmission coefficients at the three output ports versus electron energy. All dimensions such as wire widths and interguide distances are equal to 20 nm. This gives a ground quantum level at 14.1 meV which corresponds to the cutoff energy for the first propagating mode. The energy threshold for a higher-order propagating mode is 56.4 meV. In contrast to uncoupled quantum waveguides, pass- and stop-energy bands can be noticed in the transmission probability which correspond to various matching conditions of the electron wavelength to the dimension of the interconnecting branches (regions 9-5-11 for the first branch, 10-7-12 for the second). Therefore, for energy values giving rise to a standing-wave pattern along the  $y$  axis, the direct transmission  $T_{1,2}^1$  is maximum whereas the transfer from the first wire to the second is very weak, as shown in Figs. 2(b) and 2(c), where transmission spectra for ports 3 and 4 are reported. The very sharp resonant (antiresonant) peak apparent at  $E=28.2$  meV in  $T_{1,2}^1$  ( $T_{1,3}^1, T_{1,4}^1$ ) corresponds to the case where the wave function perfectly matches the two branches with a wave function vanishing at the boundaries between subregions, i.e., 9-5, 5-11, 10-7, and 7-12 interfaces, as will be the case for an infinite sidewall. As a consequence, transfer from port 1 toward port 2 is close to unity, and coupling between the two wires is forbidden. Such behavior is obtained for a third level in the  $y$  direction:

$$E_{y_3} = \hbar^2/2m * (3\pi/w)^2 = 14.1 \text{ meV}, \quad (16)$$

where  $w = 3 \times 20 \text{ nm}$  for regions 9-5-11 (and 10-7-12) combined with a first level  $E_{x_1} = 14.1 \text{ meV}$  in the  $x$  direction for a confined state in a width of  $20 \text{ nm}$ .

Turning now to an opposite situation of high transfer between the two wires, one can note that each maxima in  $T_{1,3}^i$  is split into two transmission peaks relatively close in energy as far as a monomode regime is involved. This result is a direct consequence of the dual-branch coupling scheme. Such a splitting in the transmission spectrum is a characteristic of tightly coupled quantum systems. For multiple-branch couplers one can expect that a broader

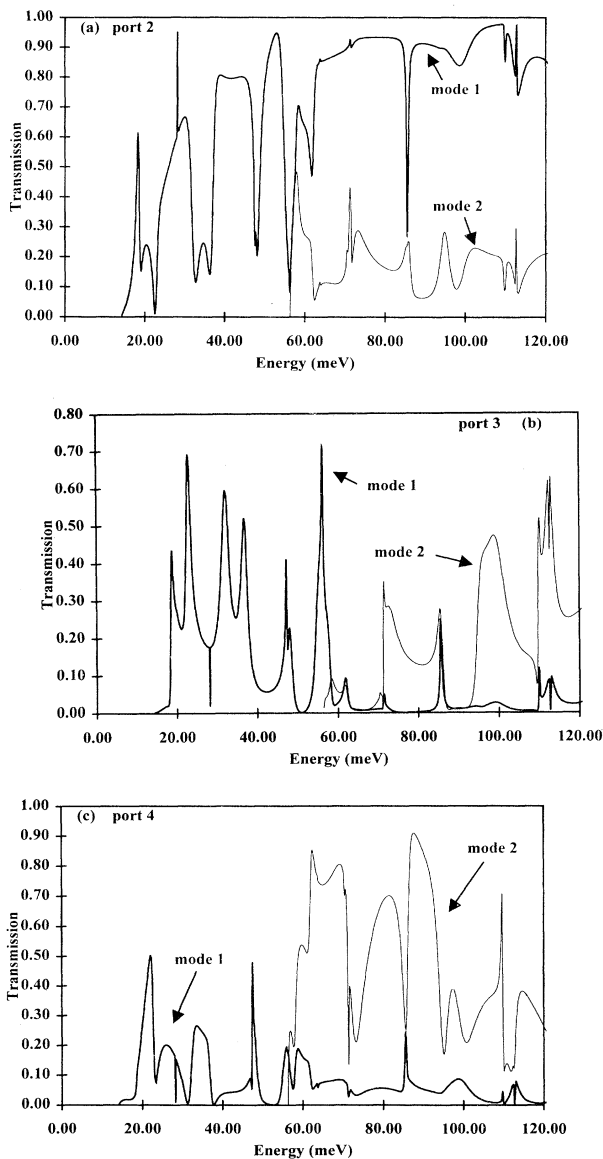


FIG. 2. Transmission spectra as a function of energy for the two first propagating modes at port 2 (a), port 3 (b), and port 4 (c) for  $L_c = L_w = 20 \text{ nm}$  (the branch widths and the interbranch distance are  $20 \text{ nm}$ ).

transmission window could thus be achieved, as is observed for finite superlattices where the strong coupling between the quantum wells gives rise to the formation of a miniband.<sup>44</sup>

To obtain insight into the directivity and coupling characteristics, it can be noted that the quantum transmission toward port 3 exceeds 50% in several cases, and that  $T_{1,3}^1$  exhibits on average higher values than  $T_{1,4}^1$ . This is an indication of the possibility to implement a highly directional coupler in the monomode regime. The situation becomes more ambiguous when two or more propagating modes are injected into the structure. Figure 2 shows that for a bimode operation the transfer between the two wires is important but that the maximum of the presence probability is now at port 4, which is characteristic of a backward wave situation.

Before studying the coupling characteristics in more detail in a multimode regime on the basis on conductance data, let us now consider the case of a coupling by evanescent waves. To this aim, the widths of the incident and transmitted waveguides have been changed to  $40 \text{ nm}$ , while the widths of the coupling branches were kept at  $20 \text{ nm}$ . The transmission coefficient between ports 1 and 3 versus energy calculated with these inputs are displayed in Fig. 3. The salient feature here is the demonstration of a relatively high transfer of electron ( $T_{13} = 0.25$ ) at an energy of  $12 \text{ meV}$ , consequently below the cutoff energy of  $14.1 \text{ meV}$  of the  $20\text{-nm}$  quantum waveguides which interconnect the two quantum wires. At higher-energy values and hence in the second-mode regime of the access waveguides a peak in the transmission can also be noted, showing the possibility to take advantage of constriction for filtering the energy for which a high level of transmissivity is observed. As a last remark concerning transmission spectra, let us note that if all characteristic dimensions had been changed to  $40 \text{ nm}$ , the results would have been equivalent to the  $20\text{-nm}$  structure, as illustrated in Fig. 2, though with an energy shift toward lower values. On the basis of this discussion, it seems preferable to design the access and interconnecting regions with comparable topology. Indeed, under these conditions, the quantum levels of each region line up and a high

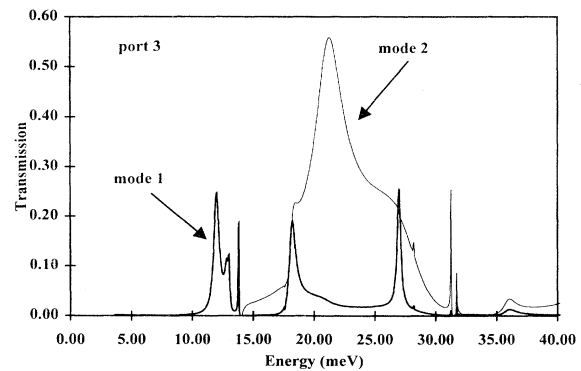


FIG. 3. Transmission spectra as a function of energy for the two first propagating modes at port 3 for  $L_c = 20 \text{ nm}$  and  $L_w = 40 \text{ nm}$  (the branch widths and the interbranch distance are  $20 \text{ nm}$ ).

transmissivity is expected. In addition, since the energy and well width are correlated, a transmission spectroscopy as a function of the well width, more directly related to experience, can be carried out. Therefore, in Sec. III B we will consider the results obtained in a conductance versus wire width approach.

### B. Conductance versus wire widths

Under the conditions of low-bias voltages and low-temperature operation, it can be assumed that there is no energy dispersion for electrons participating in the current, and hence that the energy of injection is given by the Fermi level  $E_F$  of the structure. By varying the potential of the gates which are responsible for the electron confinement by depletion, the shape and subsequently the relative position of the confinement potential with respect to  $E_F$  can be modified. In this section, we simulate a change in gate voltage by shrinking or widening the channel part under the gate. This is equivalent to an overall shift in energy of the transmission spectra. By this means the transmission properties can be investigated at the Fermi level, which is the energy reference taking advantage of the shifting of spectra when the wire width is taken as a parameter. This approach is quite similar to the method used experimentally to determine the transmission probabilities in double-barrier resonant tunneling heterostructures.<sup>45</sup> Indeed, by studying the onset of tunneling current at very low temperature, when the transmission curve begins to overlap the supply function with  $E_F$  as the energy limit, one can show that information about transmission, most notably its energy broadening, can be established. At this stage, let us define two characteristic distances we will use in the following as a function of the variables defined in Fig. 1: the wire width  $L_w$  which is equal to  $Ly_1$  and  $Ly-Ly_2$ , and the coupling length  $L_c$  which equals  $Ly_2-Ly_1$ . For the results reported hereafter, the coupling branch widths and the separation between the two branches were kept at 20 nm. Figure 4(a) shows variations of the conductance between port 1 and 2 as a function of  $L_w$  calculated for an energy reference of 40 meV. For this simulation the coupling length  $L_c$  was fixed to 20 nm whereas the widths of the incident and coupled waveguides were kept equal and varied between 10 and 60 nm. Here the conductance is expressed in units of  $2e^2/h$ . For comparison, we also plotted the variations of conductance expected for an unperturbed electron waveguide with a series of plateaus corresponding to various propagation conditions with threshold widths defined by  $L_w = M(\pi^2\hbar^2/2m^*E)^{0.5}$  ( $M=1-5$  for the width range considered). For the coupler, if the conductance quantization is preserved as a function of the number of propagating modes, the conductance evolution appears strongly perturbed by the coupling to the other waveguide, with an average conductance value lower than  $M$  times  $2e^2/h$ . On the other hand, it can be noted that a high straight-through transmission, reaching the maximum values, is recovered at each cutoff length for which a higher-order mode is accommodated. Figure 4(b) illustrates the conductances calculated for the two output ports 3 and 4, respectively.

Whatever the number of modes,  $G_3$  and  $G_4$  have comparable mean values showing that only the highest-order propagating mode participates notably in the coupling. In fact, the lowest-order modes are predominantly transmitted directly toward port 2. This means that the coupling coefficient progressively decreases as the number of propagating modes increases. Concerning the directivity, Fig. 4(b) shows that a monomode operation is a particularly favorable situation from this point of view. However, with the increase of propagating modes, it can be seen that it becomes more and more difficult to maintain significant differences between  $G_3$  and  $G_4$ , notably spike and antispikes variations as observed when only one mode can propagate. At last, as far as the conductance is concerned, one can note that all modes have quite comparable behaviors throughout their domain of appearance, except for the first mode which is in major part transmitted toward port 3.

Before considering the various modes of operation of the dual-branch coupler, it can be interesting to make a comparison between single- and double-branch schemes aimed at establishing the origin of the directivity. The results of simulations performed for this comparison are displayed in Fig. 5, which shows the wire width dependence of the conductance  $G_4$  for a reference energy of 30 meV and a coupling length of 20 nm. In the case of a

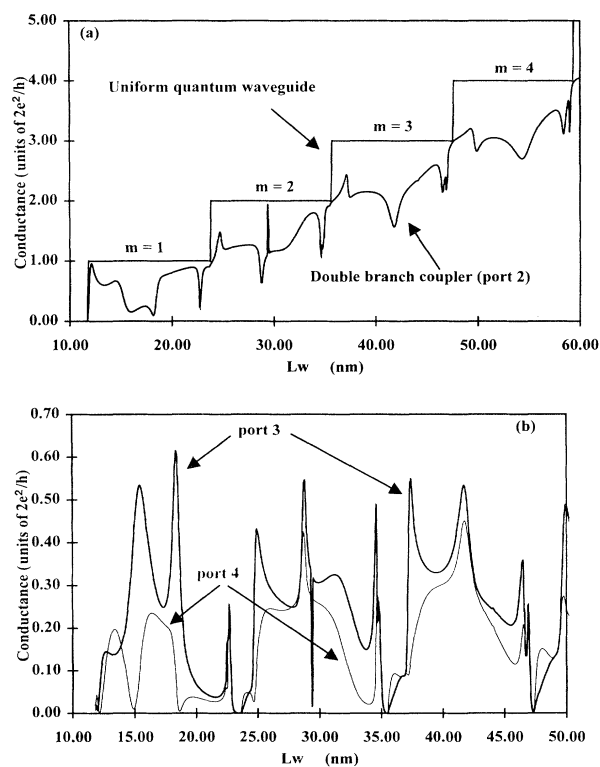


FIG. 4. Comparison of the conductance evolution between uniform quantum waveguide and the double branch coupler at port 2 (a) and conductances at port 3 and 4 for the double branch coupler (b) as a function of  $L_w$  (all other dimensions are 20 nm) for an incident energy  $E = 40$  meV.

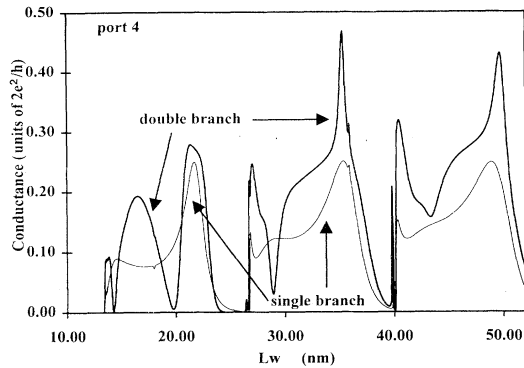


FIG. 5. Comparison of  $G_4$  between a single-branch coupler and a double-branch coupler for  $E = 30$  meV as a function of  $Lw$  (all other dimensions are 20 nm).

single-branch structure, the calculation of  $G_3$  and  $G_4$  shows that there are only slight differences in the variations between them as a function of  $Lw$ . Hence no directivity effect can be pointed out. Indeed let us recall that the size of the coupling window is at the scale of 20–40 nm in order to promote transverse quantum effects in the interconnecting region. This also means that the ways to couple ports 3 and 4 to the incident port 1 are quite similar at the scale of the opening chosen here. On the contrary, marked differences can be pointed out in the transmission as seen before, and hence in the conductance variations between ports 3 and 4 for a double-branch configuration. It is clear that to couple a wire by means of two distinct paths introduces phase shifts between the wave-function contributions leading to marked interference phenomena. In analogy with microwave couplers, one can also imagine an increase in the number of coupling branches. In that case one can expect the same advantage afforded by the multiplicity of coupling structures for electromagnetic couplers notably in terms of frequency (energy) band. However, we have to keep in mind that the observation of the interference described here needs to preserve a ballistic transport during the coupling process. An increasing number of branches should enhance the probabilities of phase breaking, with the result of strong modifications in transmission spectra.

### C. Coupling length and bias voltage

Another parameter of key importance is the coupling length  $L_c$  between the two parallel waveguides. First of all, the same trends in the conductance variations are observed if  $L_c$  is chosen as a multiple of the previous value  $L_c = 20$  nm. In this case, higher-order modes can be accommodated over the coupling length but, on the whole, the interference pattern remains unchanged. On the contrary, by varying the value of  $L_c$  without keeping a periodicity rule, various operation regimes can be observed, as is exemplified in Fig. 6 which shows the variations of conductance versus the wire width calculated at the three ports 2, 3, and 4 for  $L_c = 50$  nm. Three regimes can be pointed out in the wire width window which corresponds to a monomode regime. First of all, for

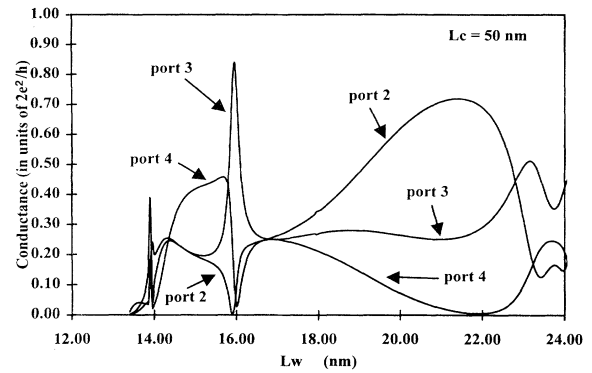


FIG. 6. Evolution of the conductance at the output ports of the structure for a coupling length  $L_c = 50$  nm as a function of  $Lw$  at  $E = 30$  meV (branch widths and interbranch distance are fixed to 20 nm).

$Lw = 16$  nm, a quasicomplete transfer of the presence probabilities between ports 1 and 3 with negligible values at the two other ports is apparent. In contrast to this, we obtained a regime of equal sharing of the presence probabilities for  $Lw \sim 17$  nm, where equal conductance levels are calculated at all ports. Finally, one can note that the charge transfer toward port 4 can be inhibited over a relative wire width range in the vicinity of  $Lw = 22$  nm.

Let us now consider the effect of a drain-source voltage bias. To this aim, a very simple model has been considered which assumes a uniform field in the interconnecting regions and a steplike distribution of potential along  $x$  to describe the voltage drop across the structure with respect to the flat conditions assumed previously for the calculations. In practice for a given voltage  $V_{tot}$ , a constant electrostatic potential is considered in each region. Therefore, the potential is set to 0 V for regions 1 and 4,  $-V_{tot}/4$  in regions 9, 5, and 11,  $-V_{tot}/2$  in regions 6 and 8,  $-3V_{tot}/4$  in regions 10, 7, and 12, and  $-V_{tot}$  in regions 2 and 3. Using this approach, the mode-matching technique can be directly applied, taking into account the correction of propagating or attenuating factors in each region due to the change in the reference energy. It is worth mentioning that this procedure is no longer valid when the energy values gained at each boundary region exceeds the values of eigenstates of the wells in that case introducing a nonrealistic confinement potential. Figure 7 shows the transmission spectrum for the first propagating mode between ports 1 and 3 at equilibrium and under bias voltages of 4 and 10 mV. In this structure, all characteristic dimensions are kept constant at 20 nm. As is observed in devices making use of quantum-size effects such as double-barrier heterostructures, the resonant and antiresonant structures are shifted toward lower values at increasing bias. This can be explained by the lowering of the quantum states of the interaction region relative to the injection region. In addition, one can note less efficient resonant effects as a direct consequence of the asymmetry in the structure introduced by the applied voltage.<sup>46</sup> Here again the analogy with the resonant double barrier is fruitful, for which

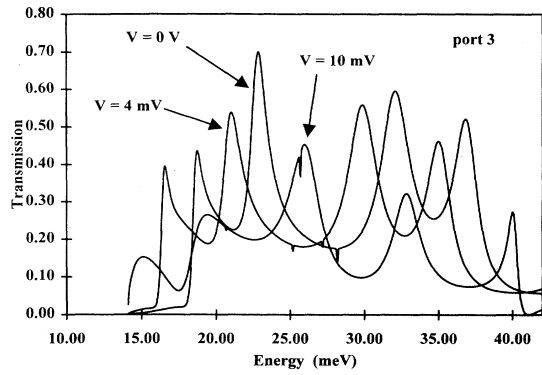


FIG. 7. Transmission spectra at port 3 as a function of energy for various bias conditions in the  $x$  direction (all dimensions are fixed to 20 nm).

quite similar effects can be pointed out under bias. In fact, the mismatch between the quantum levels in the incident or transmitted quantum wires is progressively misaligned, and as a consequence the resonant transport tends to become smeared.

#### D. Coupling parameters and wave functions

By means of Eqs. (14) and (15), the directivity ( $D$ ) and the coupling coefficient ( $C$ ) can be calculated for various energy and operating conditions. As an example, Fig. 8 shows the variations of  $D$  and  $C$  versus  $Lw$  for an incident-energy value of 20 meV. Over the well width investigated, the directivity in most cases appears positive and hence with a preferential transfer toward port 3. The highest value ( $D \sim 30$  dB) was obtained in a fundamental propagating mode regime just before the wire width, at which another mode starts to carry current. As expected from the previous analysis, in a multimode regime the directivity is lowered, with maximum values around 12 dB. Concerning the coupling characteristics, one can note that  $C$  exceeds the reference value of 3 dB plotted in dotted lines at  $Lw = 24$  nm. In that particular case,  $C$  is close to 0 dB, corresponding to full transfer conditions. Otherwise a 3-dB coupler (in analogy with the hybrid microwave coupler) can be implemented with a directivity

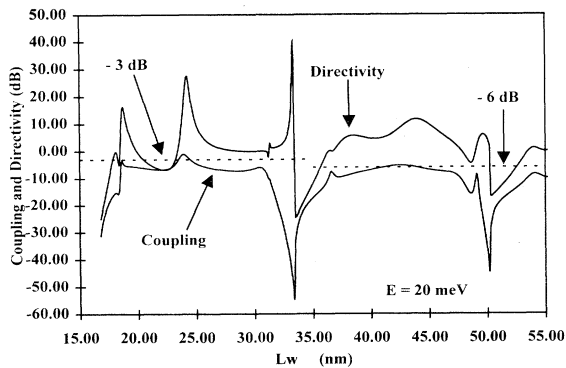


FIG. 8. Calculated coupling coefficient and directivity as a function of  $Lw$  for  $E = 20$  meV (all other dimensions are 20 nm).

starting from 15 up to 35 dB in the 20–40-meV energy range. In agreement with the arguments developed in Sec III B the coupling values are lowered when two current-carrying modes are assumed. Under these conditions the maximum data are close to 6 dB, this reference value being plotted in dotted lines. On this basis, a systematic study can be undertaken by systematically vary-

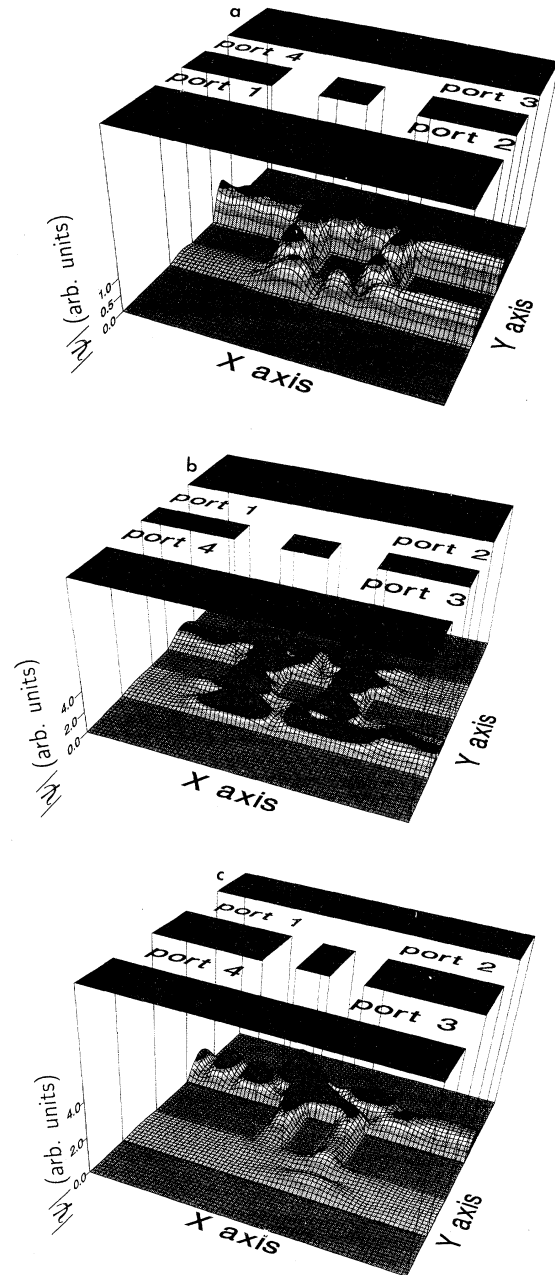


FIG. 9. Operating regimes for the double branch quantum coupler for different geometrical designs (the branch widths and the interbranch distance are fixed to 20 nm). (a) 3 dB coupling:  $E = 31.5$  meV,  $Lw = 20$  nm, and  $Lc = 20$  nm. (b) Real-space transfer:  $E = 30$  meV,  $Lw = 27.4$  nm, and  $Lc = 15$  nm. (c) Coupling by evanescent wave:  $E = 30$  meV,  $Lw = 40$  nm, and  $Lc = 60$  nm.

ing the topology of the structures in order to optimize coupling and directivity characteristics. Four representative results of this parametric study are given in Figs. 9(a), 9(b), and 9(c).

Figure 9(a) gives a three-dimensional view of the modulus of the wave function (instead of the squared modulus for the sake of clarity in the drawing) within a structure for an injected energy of 31.5 meV and for all dimensions equal to 20 nm. An equal sharing of the presence probability is apparent at the output ports 1 and 3 along with a low reflection coefficient at the feeding port 1 (lower than 0.01, here characterized by smooth oscillations of the wave function above 1). Conversely, the value of  $T_{14}^1$  is less than 0.005. Such a low transmissivity can be understood by the rapid decay in the wave function due to the excitation of higher-order evanescent modes for the energy considered (here a node in the middle of the channel in the  $y$  direction at the interface 11-4). On the other hand, the equal partition in the output wires 2 and 3 can be explained by the balance between the direct transmission from port 1 toward port 2 and the extracted electron fluxes at each branch which recombine constructively in the third output wire. The low reflectivity at port 1 and also the efficient coupling to the second wire can be explained by an antinode in the modulus of the wave function in the vicinity of the cross between the incident wire and the branch lines.

For the two examples displayed in Figs. 9(b) and 9(c), the energy injection was fixed to 30 meV and the distance between the two branches kept at 20 nm. However, the coupling length  $Lc$  and the input and output wire widths were varied in order to change the wave-function configuration. Figure 9(b) corresponds to  $Lc=15$  nm and  $Lw=27.4$  nm. For these input data a complete charge transfer between ports 1 and 3 ( $G_3=0.943 \times 2e^2/h$ ) is obtained. This behavior stems from the fact that the scattered waves are in phase in port 3, explaining a high transmissivity, and out of phase in port 2, where the wave function is quenched. In contrast to this, as  $Lw$  is set to 29 nm, a straight-through transmission ( $G_2=0.993 \times 2e^2/h$ ) can be achieved. By taking advantage of straight-through and real-space transfer regimes the concept of a switching action relying entirely on quantum interference can be supported. In addition, if we view the transfer of electrons from one wire to the other as a resonant process, an estimate of the characteristic time of this switching mechanism can be found. Indeed, the width at half maximum of the peak of transmission as a function of energy can be related to the dwell time within the coupling region:  $\tau=\hbar/\Gamma$ . On this basis, we found  $\Gamma=1.2$  meV or  $\tau=0.55$  ps, which validates the expectation of a very fast transfer.

Finally, Fig. 9(c) corresponds to a coupling by an evanescent mode. This operating regime was pointed out in Sec. III B for a topology corresponding to wire widths equal to 40 nm and to branch-line widths equal to 20 nm. In order to investigate where the electrons go, the cou-

pling length was fixed to 60 nm so that the evanescence of the electron wave, generated below the cutoff energy of the interconnecting waveguides, can be demonstrated unambiguously. For waveguides in closer proximity it is clear that this coupling by evanescent modes, and hence similar to a tunneling regime, could be strengthened.

#### IV. CONCLUSION

In summary, we have investigated theoretically the potential of a dual-branch coupling scheme between two electron waveguides. Ballistic transport conditions are assumed so that the conduction characteristics are solely determined by the structure geometry. For this analysis, we have developed a numerical code based on mode-matching techniques for solving the two-dimensional Schrödinger equation in a multiple-port configuration. This method was successfully applied to the quantum coupler proposed including 20 modes (evanescent or propagating) in the simulations, and was systematically used to calculate the quantum transmission probabilities and the conductance characteristics. As the topology of structures is varied, several kinds of coupling characteristics have been pointed out, taking benefit of the quantum interferences which develop in the interconnecting regions including (i) straight-through transmission; (ii) multiplexing of the presence probabilities with an equal partition between two output ports, whereas the wave function collapses at the fourth port; or (iii) full electron transfer between the two-electron waveguides. As a general rule, and as expected, the most salient features have been obtained in a monomode propagation regime. For instance, in a structure where the wire dimension is close to 20 nm, a 3-dB coupling coefficient along with a directivity of 35 dB was obtained. When several current-carrying paths are allowed, as is the case in multimode operation, the directional coupling still holds, though with degraded performances in terms of coupling (6 dB) and directivity (10 dB), characteristics due to the straight-through transmission of low-energy-relying modes. On the other hand, using an open-coupling window instead of a tunneling barrier appears to be a welcome feature if we are interested in the time response properties. Preliminary estimates of the dwell time within the active region using the width at half maximum of the quantum transmission probabilities versus energy show that the transfer of charge can occur with about a half-picosecond time response in a switching process. On this basis and in anticipation of future improvements in the fabrication techniques and higher quality material, it is believed that this class of quantum components can find application in extremely low consumption and ultrafast devices. As a last comment, let us note that a further degree of control can be afforded by the application of a magnetic field, as is observed for Aharonov-Bohm rings for which strong interference phenomena have been predicted and clearly demonstrated in experiment.<sup>47,48</sup>

- <sup>1</sup>L. Esaki and R. Tsu, *IBM J. Res. Dev.* **14**, 61 (1970).
- <sup>2</sup>R. Tsu and L. Esaki, *Appl. Phys. Lett.* **22**, 562 (1973).
- <sup>3</sup>*Resonant Tunneling in Semiconductors: Physics and Applications*, edited by L. L. Chang, E. E. Mendez, and C. Tejedor (Plenum, New York, 1991).
- <sup>4</sup>L. Burgnies, O. Vanbésien, V. Sadaune, D. Lippens, J. Nagle, and B. Vinter, *J. Appl. Phys.* **75**, 4527 (1994).
- <sup>5</sup>J. S. Scott, J. P. Kaminski, M. Wanke, S. J. Allen, D. H. Chow, M. Lui, and T. Y. Liu, *Appl. Phys. Lett.* **64**, 1995 (1994).
- <sup>6</sup>M. A. Reed, J. N. Randall, R. J. Aggarwal, R. J. Matyi, T. M. Moore, and A. E. Wetsel, *Phys. Rev. Lett.* **60**, 535 (1988).
- <sup>7</sup>J. P. Eisenstein, L. N. Pfeiffer, and K. W. West, *Appl. Phys. Lett.* **58**, 1497 (1991).
- <sup>8</sup>M. Sumetskii, *Appl. Phys. Lett.* **63**, 3185 (1993).
- <sup>9</sup>G. W. Bryant, *Phys. Rev. B* **39**, 3145 (1989).
- <sup>10</sup>S. Tarucha, Y. Hirayama, and Y. Tokura, *Appl. Phys. Lett.* **58**, 1623 (1991).
- <sup>11</sup>J. N. Randall, A. C. Seabaugh, Y. C. Kao, J. H. Luscombe, and B. L. Newell, *J. Vac. Sci. Technol. B* **9**, 2893 (1991).
- <sup>12</sup>J. W. Sakai, P. C. Main, P. H. Beton, N. La Scala, Jr., A. K. Geim, L. Eaves, and M. Henini, *Appl. Phys.* **64**, 2563 (1994).
- <sup>13</sup>K. Hirakawa and H. Sakaki, *Phys. Rev. B* **33**, 8291 (1986).
- <sup>14</sup>D. A. Wharam, T. J. Thornton, R. Newbury, M. Pepper, H. Ahmed, J. E. F. Frost, D. G. Hasko, D. C. Peacock, D. A. Ritchie, and G. A. C. Jones, *J. Phys. C* **21**, L209 (1988).
- <sup>15</sup>G. Timp, A. M. Chang, P. Mankiewich, R. Behringer, J. E. Cunningham, T. Y. Chang, and R. E. Howard, *Phys. Rev. Lett.* **59**, 732 (1987).
- <sup>16</sup>B. J. van Wees, L. P. Kouwenhoven, E. M. M. Willems, C. J. P. Harmans, J. E. Mooij, H. van Houten, C. W. J. Beenakker, J. G. Williamson, and C. T. Foxon, *Phys. Rev. B* **43**, 12431 (1991).
- <sup>17</sup>K. Nakazato, T. J. Thornton, J. White, and H. Ahmed, *Appl. Phys. Lett.* **61**, 3145 (1992).
- <sup>18</sup>S. Y. Chou and Y. Wang, *Appl. Phys. Lett.* **63**, 788 (1993).
- <sup>19</sup>J. C. Wu, M. N. Wybourne, W. Yindepol, A. Weisshaar, and S. M. Goodnick, *Appl. Phys. Lett.* **59**, 102 (1991).
- <sup>20</sup>J. C. Wu, M. N. Wybourne, C. Berven, S. M. Goodnick, and D. D. Smith, *Appl. Phys. Lett.* **61**, 2425 (1992).
- <sup>21</sup>S. M. Goodnick, J. C. Wu, M. N. Wybourne, and D. D. Smith, *Phys. Rev. B* **48**, 9150 (1993).
- <sup>22</sup>Y. S. Joe and S. E. Ulloa, *J. Appl. Phys.* **74**, 4892 (1993).
- <sup>23</sup>Z. Shao, W. Porod, and C. S. Lent, *Phys. Rev. B* **49**, 7453 (1994).
- <sup>24</sup>D. Jovanovic and J. P. Leburton, *Phys. Rev. B* **49**, 7475 (1994).
- <sup>25</sup>R. A. Wyss, C. C. Eugster, J. A. del Alamo, and Q. Hu, *Appl. Phys. Lett.* **63**, 1522 (1993).
- <sup>26</sup>Y. Feng, A. S. Sachrajda, R. P. Taylor, J. A. Adams, M. Davies, P. Zawadzki, P. T. Colridge, D. Landheer, P. A. Marshall, and R. Barber, *Appl. Phys. Lett.* **63**, 1666 (1993).
- <sup>27</sup>R. L. Schult, D. G. Ravenhall, and H. W. Wyld, *Phys. Rev. B* **39**, 5476 (1989).
- <sup>28</sup>Y. Takagaki and D. K. Ferry, *Phys. Rev. B* **45**, 13494 (1992).
- <sup>29</sup>F. Sols, M. Maccuci, U. Ravaioli, and K. Hess, *J. Appl. Phys.* **66**, 3892 (1989).
- <sup>30</sup>C. C. Eugster, J. A. del Alamo, M. J. Rooks, and M. R. Melloch, *Appl. Phys. Lett.* **60**, 642 (1992).
- <sup>31</sup>C. C. Eugster, J. A. Del Alamo, M. J. Rooks, and M. R. Melloch, *Appl. Phys. Lett.* **64**, 3157 (1994).
- <sup>32</sup>G. Xu, M. Yang, and P. Jiang, *J. Appl. Phys.* **74**, 6747 (1993).
- <sup>33</sup>J. Wang and H. Guo, *Phys. Rev. B* **48**, 12072 (1993).
- <sup>34</sup>Y. Takagaki and K. Ploog, *Phys. Rev. B* **49**, 1782 (1994).
- <sup>35</sup>H. U. Baranger, *Phys. Rev. B* **42**, 11479 (1990).
- <sup>36</sup>E. Kühn, *Arch. Elek. Übertragung* **27**, 511 (1973).
- <sup>37</sup>A. Weisshaar, J. Lary, S. M. Goodnick, and V. K. Tripathi, *Appl. Phys. Lett.* **55**, 2114 (1989).
- <sup>38</sup>A. Weisshaar, J. Lary, S. M. Goodnick, and V. K. Tripathi, *J. Appl. Phys.* **70**, 355 (1991).
- <sup>39</sup>R. Landauer, *Philos. Mag.* **21**, 863 (1970).
- <sup>40</sup>M. Büttiker, *Phys. Rev. Lett.* **57**, 1761 (1986).
- <sup>41</sup>O. Vanbésien and D. Lippens, *Appl. Phys. Lett.* **65**, 2439 (1994).
- <sup>42</sup>O. Vanbésien and D. Lippens, *Superlatt. Microstruct.* (to be published).
- <sup>43</sup>O. Vanbésien, D. Wojciechowski, V. Sadaune, and D. Lippens, in *Physics of Semiconductor Devices*, edited by K. Lal (Narosa, New Delhi, 1993).
- <sup>44</sup>O. Vanbésien, H. Leroux, and D. Lippens, *Solid-State Electron.* **35**, 665 (1992).
- <sup>45</sup>M. Tsuchiya and H. Sakaki, *Jpn. J. Appl. Phys.* **30**, 1164 (1991).
- <sup>46</sup>B. Ricco and M. Azbel, *Phys. Rev. B* **29**, 1970 (1984).
- <sup>47</sup>M. Büttiker, *Phys. Rev. B* **33**, 3020 (1986).
- <sup>48</sup>P. J. Simpson, D. R. Mace, C. J. B. Ford, I. Zailer, M. Pepper, D. A. Ritchie, J. E. F. Frost, M. P. Grimshaw, and G. A. C. Jones, *Appl. Phys. Lett.* **63**, 3191 (1993).

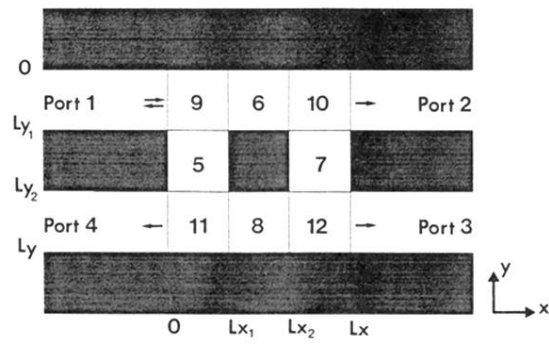


FIG. 1. Topology of the quantum directional coupler with two branch lines.

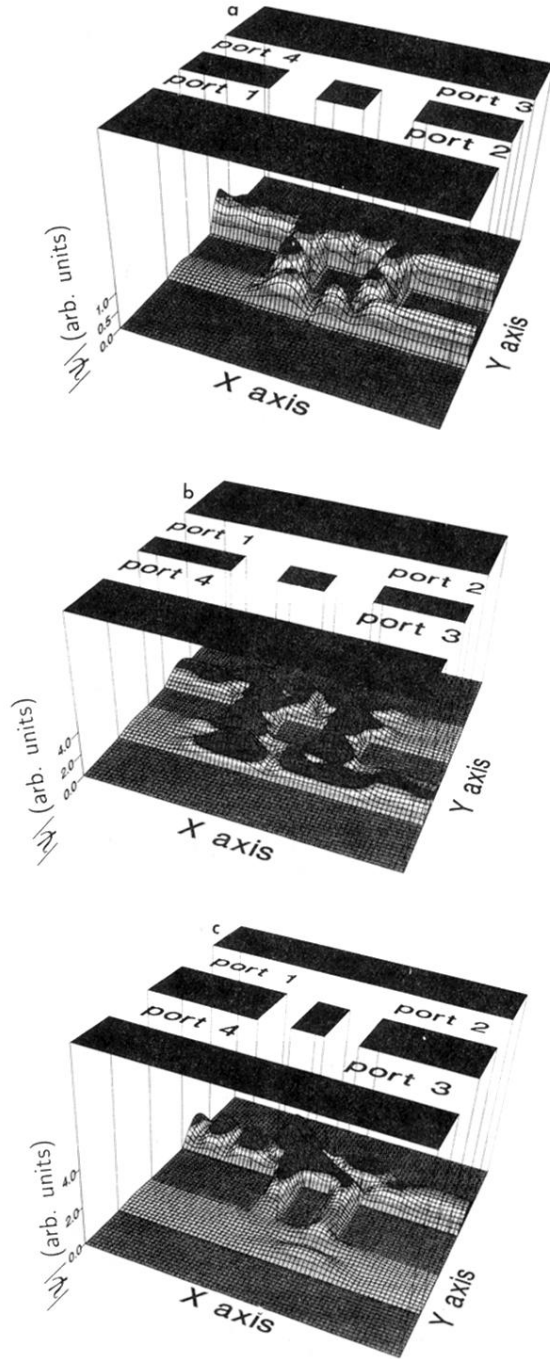


FIG. 9. Operating regimes for the double branch quantum coupler for different geometrical designs (the branch widths and the interbranch distance are fixed to 20 nm). (a) 3 dB coupling:  $E = 31.5$  meV,  $Lw = 20$  nm, and  $Lc = 20$  nm. (b) Real-space transfer:  $E = 30$  meV,  $Lw = 27.4$  nm, and  $Lc = 15$  nm. (c) Coupling by evanescent wave:  $E = 30$  meV,  $Lw = 40$  nm, and  $Lc = 60$  nm.